Research Article

Enran Hou, Umar Nazir, Muhammad Sohail*, and Thabet Abdeljawad*

Significance of 3D rectangular closed domain filled with charged particles and nanoparticles engaging finite element methodology

https://doi.org/10.1515/phys-2024-0073
received February 22, 2024; accepted July 26, 2024

Abstract: This article aims to use passive flow control to analyze the transportation of heat, mass, and charged particles toward a 3D plate. The current problem offers a novel exploration of the flexible domain of non-Newtonian materials, which are well known for their wide range of applications in the engineering and industrial domains. The current study explores the complex dynamics of heat and mass transfer in a fluid that flows over an elongating sheet. The motion of the nanofluid on the surface is caused by the stretching of the 3D plate. The suspension of mixtures of tetra-hybrid nanoparticles can enhance thermal performance and cooling mechanism. Moreover, the 3D model includes modeling of multiple important parameters, such as heat source, thermal radiation, and Hall and Ion slip effects, in Cartesian coordinates for a three-dimensional stretched plate. This comprehensive analysis of various effects offers a new perspective to the field. Partial differential equations represent the emergent phenomena in the problem formulation process. It was estimated that an enhancement of charged particles and motion regarding nanoparticles is enhanced *versus* an enhancement of charged particles. With the greater power law index, suction, and Weissenberg number, the acceleration of nanoparticles is enhanced.

Keywords: charged particles, solar thermal radiation, complex fluid, tetra-hybrid nanoparticles, heat sink, 3D surface, engine oil

*** Corresponding author: Muhammad Sohail,** Institute of Mathematics, Khwaja Fareed University of Engineering & Information Technology, Rahim Yar Khan 64200, Pakistan; Composite Materials Scientific Research Center of Azerbaijan State University of Economics (UNEC), 194 Murtuza Mukhtarov Street, Baku, AZ1065, Azerbaijan, e-mail: muhammad_sohail111@yahoo.com
*** Corresponding author: Thabet Abdeljawad,** Department of Mathematics and Sciences, Prince Sultan University, Riyadh, Saudi Arabia; Department of Medical Research, China Medical University, Taichung, 40402, Taiwan; Department of Mathematics and Applied Mathematics School of Science and Technology, Sefako Makgatho Health Sciences University, Ga-Rankuwa, South Africa, e-mail: tabdeljawad@psu.edu.sa
Enran Hou: School of Mathematics and Statistics, Huaibei Normal University, 235000, Huaibei, China
Umar Nazir: Department of Mathematics, Faculty of Science, Khon Kaen University, Khon Kaen, 40002, Thailand

Nomenclature

a	constant
Al_2O_3	aluminum oxide
A_{sr}	irradiance factor
B_0	magnetic field
B_e	Hall number
B_i	ion slip number
c	concentration (mol m^{-3})
c_{Fx}, c_{Fg}	skin friction coefficients
c_P	specific heat capacitance (J kg^{-1} K^{-1})
$(c)_\infty$	ambient concentration (mol m^{-3})
$(c)_W$	wall concentration (mol m^{-3})
D	mass diffusion (m^2 s^{-1})
E	activation energy number
E_0	activation energy at zero
F, G	dimensionless velocity fields
F_w	dimensionless suction velocity
Fe_3O_4	iron dioxide
H_t	heat source number
k	thermal conductivity (W m^{-1} k^{-1})
k_e	dimensional chemical reaction parameter
O_1, O_3, O_4, O_2	volume fractions of nanofluid
Cu	copper
Ec	Eckert number
EO	engine oil
FEM	finite element method
GFEA	Galerkin finite element approach
Ha	Hartmann number
hB	hybrid nanofluid
n	power law index number

Nu	Nusselt number
ODEs	ordinary differential equations
Pr	Prandtl number
Q_{sr}	irradiance factor
Re	Reynolds number
Sc	Schmidt number
Sh	Sherwood number
TiO_2	titanium dioxide
T_0	reference temperature (K)
tN	tetra-hybrid nanofluid
Tri	tri-hybrid nanofluid
T	temperature (K)
$(T)_\infty$	ambient temperature (K)
$(T)_\mathbb{W}$	wall temperature (K)
ν	kinematic viscosity ($m^2\ s^{-1}$)
We	Weissenberg number
Y, X, Z	space coordinates ($m\ s^{-1}$)
σ	electrical thermal conductivity ($kg\ m^{-3}$)
Γ	time relaxation number (s)
∞	infinity
η	independent variable
Θ	dimensionless temperature
Φ	dimensionless concentration
$\mathbb{U}, \mathbb{V}, \mathbb{W}$	velocity fields ($m\ s^{-1}$)
ρ	density ($kg\ m^{-3}$)
η_{max}	Independent variable at maximum domain

1 Introduction

Because of their applications, non-Newtonian fluids have been the subject of in-depth research by numerous scholars. Jamshed *et al.* [1] numerically computed the magnetized Powell Eyring nano liquid with the utilization of a single-phase model. Finite element analysis based on cross fluid induced by vertical disk exposed to tetra hybrid nanosize particle mixture dispersion was discussed by Sohail *et al.* [2]. Waseem *et al.* [3] analyzed the entropy approach concerning magnetized hybrid nanosize particles by invoking the optimal homotopy analysis method technique. Moreover, Waseem *et al.* [4] also analyzed the entropy production appertaining to 3D expanded magnetically driven hybrid nanofluid influenced by thermal radiation along with heat generation impacts. Statistical analysis and morphological features concerning rheological materials dispersed in the transmission of silica, titanium, alumina, and also ethylene glycol with the utilization of Galerkin methodology were captured by Li *et al.* [5]. Entropy theory and Powell–Eyring hybrid nanofluidic with heat dissipation were reported by Aziz *et al.* [6]. A comparative study proffered by Jamshed *et al.* [7] based on inclined magnetically driven Powell-Eyring Nano liquid induced by nonuniformly rotating expanded flat surface. A theoretical investigation was conducted by Avramenko *et al.* [8] based on fluid occurrence and also heat transfer across the boundary layer subjected to surface. Efficiency appertains to thermal energy as well as solute particles with the utilization of hybrid nanosize particles influenced by chemical reaction along with activation energy exposed to the parabolic surface, which was studied by Chu *et al.* [9]. In this study, the finite element approach was opted. Akram *et al.* [10] explored the hybridized consequences concerning thermal as well as concentration convection based on peristaltic transmission magnetized Powell–Eyring nano liquids configured by slanted an asymmetric channel. Aziz *et al.* [11] modeled and also simulated the 3D magnetized spinning water-reliant multi wall carbon nanotubes nano fluidic flow demeanor by invoking convective prior conditions as well as slip impacts. Patil *et al.* [12] have examined the unsteady magnetized in terms of thermal radiation and chemical response nano Powell-Eyring liquid close to the stagnation point bounded by a convectively heated extending sheet. A 3D Casson fluid model under consideration of temperature-reliant conductance *via* shooting technique was discussed by Sohail *et al.* [13]. Moreover, Joule heating along with viscous dissipation impacts also contributed to this study. Radial magnetized non-Newtonian fluidic occurrence by utilizing an advanced heat flux model influenced by Joule heating was reported by Sohail *et al.* [14]. Waqas *et al.* [15] numerically analyzed the convected occurrence based on Oldroyd-B nano liquid in the presence of motile organisms together with thermal radiation configured by a spinning disk. Song *et al.* [16] discussed the advanced Darcy law and also nonlinear thermal radiation applications rely on bio-convected occurrence referring to micropolar nano liquid bounded by rotating disk. Thermal conductivity performance is relevant to the convected flow demeanor of cross nano fluid comprising swimming microorganisms induced by a cylinder exposed to melting phenomenon, which was numerically evaluated by Imran *et al.* [17]. Binary-band nonreciprocal thermal radiation under coupling of optical Tamm conditions within the magnetophotonic multilayers was reported by Wu *et al.* [18]. Owing to the attractive broad applications of borophene, Super-Planckian thermal radiation was examined by Zhou *et al.* [19] across the borophene sheets. The Williamson fluid model was studied by Khan *et al.* [20] in terms of blood-carrying gold nano-size particles subjected to curved surfaces under significant effects of thermal radiation, suction, and also Lorentz force. Computational analysis was performed by Imran *et al.* [21] appertains to nanosized particles shape toward the hybrid nano fluidic occurrence owing to the plate with solar radiation. Moreover,

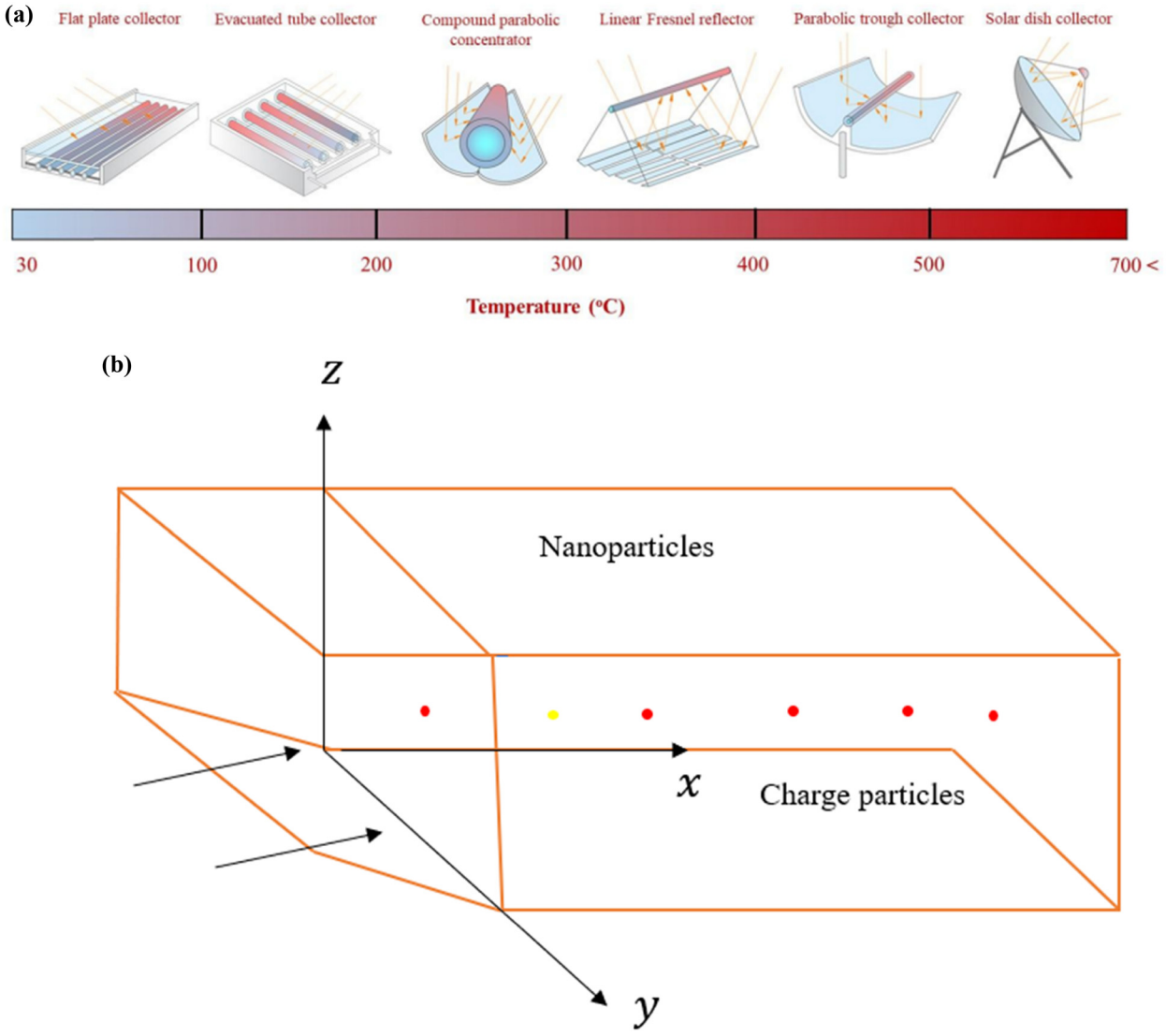

Figure 1: (a) Different technologies of solar radiation consider temperature ranges. (b) Physical model and coordinates system.

Imran *et al.* [22] also studied the physical attributes based on bio-convection toward the nano liquid flow demeanor across a paraboloid of revolution bounded by horizontal surface exposed to motile organisms. Entropy production was scrutinized by Farooq *et al.* [23] across the magnetized nano liquid occurrence under consideration of nonlinear thermal radiation. Buoyancy convected flow demeanor and also heat dissipation of nano size liquids across the annulus possessing a thin baffle were studied by Pushpa *et al.* [24]. The entropy approach together with the thermal transmission of Cu-water nano-fluid within the penetrating lid-driven cavity in terms of magnetic field was discussed by Marzougui *et al.* [25]. A statistical approach was conducted by Shafiq *et al.* [26] in terms of dual stratification across the stagnation point Walter's B Nano fluidic occurrence through a radial Riga plate. Numerical as well as series solutions were obtained by Mushtaq *et al.* [27] relying on Powell–Eyring liquid *via* exponentially extending sheet. Figure 1a displays several varieties of solar thermal collectors, such as parabolic troughs, linear Fresnel reflectors, compound parabolic concentrators, flat plate collectors, collectors with evacuated tubes, and concentrating solar dishes. Abrar *et al.* [28] looked into the micro-rotation effects of a tangent hyperbolic hybrid nanofluid flowing across a porous sheet. By utilizing the shooting approach in conjunction with (RKF-45), one can achieve the numerical simulations to leading differential equations. The physical meaning of the essential characteristics is obtained *via* graphic results. Samad Khan *et al.* [29] investigated the entropy produced by the micro-rotation of Casson's nanofluid and the impact of a magnetic field flowing through a nonlinear stretched surface. When designing a mechanical

system that depends on heat transport, entropy minimization is crucial. An exponentially expanding convective wall is used to study the rheology of silver and alumina nanoparticles by Abrar et al. [30,31]. Internal heat generation and absorption impact when a magnetic field is applied. The impact of an angled magnetic field (MG) on the formation of entropy in a Jeffery nanofluid flow across a stretching surface with viscous dissipation was examined by Akhtar *et al.* [32]. In a flexible circular duct that is axisymmetric within the walls of the cilia, Abrar *et al.* [33] explored the peristaltic transfer of nanofluid. In all cases when solid nanoparticles are taken into consideration, the temperature profile drastically reduces as the radiation parameter rises. Li *et al.* [34] estimated the aspects of the Eyring liquid with the suspension of partial ionization on rotating disks. They have assumed thermophoretic deposition (particles) resolved numerically with double diffusion. Das *et al.* [35] studied thermos-diffusion and thermal energy on the surface visualizing thermal transport and thermal radiation. Hall currents, magnetic force, and Hall currents were assumed. Ali *et al.* [36] analyzed the character of ternary hybrid nano-martial in Casson nanofluid considering Coriolis force, Hall currents, buoyancy force, and rotating plate were assumed. Different technologies of solar radiation consider temperature ranges as shown in Figure 1a.

In published works, investigation regarding three-dimensional flows in tetra-hybrid nanofluid is not documented well. This artice is organized as follows: The model's formulation is covered in Section 2. Section 4 presents the analysis of the results, while Section 3 covers the methodology of the numerical approach. Section 5 discusses important points.

2 Mathematical procedure and statement

Thermal and concentration performances of complex fluid on 3D surfaces are carried out. Advanced correlations regarding tetra-hybrid nanofluid are developed using a mixture of copper, Al_2O_3, iron dioxide, and TiO_2 in engine oil (EO). The partially ionizations are inserted into mixtures of nanoparticles. The developed mixture over 3D surface is induced with wall velocity $[a(X + Y, b(Y + X)]$, where b and a are constants. Energy equation contains solar thermal radiation and heat sink/absorption with the suspension of four kinds of nanoparticles, while the term regarding activation energy is added to the concentration equation. The physical development of the model is considered in Figure 1b. A set associated with partial differential equations [37,38] is obtained:

$$(\mathbb{U})_X + (\mathbb{W})_Z + (\mathbb{V})_Y = 0, \tag{1}$$

$$\begin{aligned}\mathbb{U}(\mathbb{U})_X + \mathbb{V}(\mathbb{U})_Y + \mathbb{W}(\mathbb{U})_Z &= \frac{(B_0)^2 \varrho_{\mathrm{tN}}}{\rho_{\mathrm{Thnf}}[(1 + B_{\mathrm{i}}B_{\mathrm{e}})^2 + (\beta_{\mathrm{e}})^2]}[\mathbb{V}B_{\mathrm{e}} - (1 + B_{\mathrm{i}}B_{\mathrm{e}})\mathbb{U}] \\ &+ \nu_{\mathrm{tN}}\left[(1 - n)\mathbb{U}_{ZZ} + n(2)^{\frac{1}{2}}\Gamma\mathbb{U}_Z\mathbb{U}_{ZZ}\right],\end{aligned} \tag{2}$$

$$\begin{aligned}\mathbb{U}(\mathbb{V})_X + \mathbb{V}(\mathbb{V})_Y + \mathbb{W}(\mathbb{V})_Z &= -\frac{(B_0)^2 \varrho_{\mathrm{tN}}}{\rho_{\mathrm{tN}}[(1 + B_{\mathrm{i}}B_{\mathrm{e}})^2 + (\beta_{\mathrm{e}})^2]}[\mathbb{U}B_{\mathrm{e}} + (1 + B_{\mathrm{i}}B_{\mathrm{e}})\mathbb{V}] \\ &+ \nu_{\mathrm{tN}}\left[(1 - n)\mathbb{V}_{ZZ} + n(2)^{\frac{1}{2}}\Gamma\mathbb{V}_Z\mathbb{V}_{ZZ}\right],\end{aligned} \tag{3}$$

$$\begin{aligned}\mathbb{U}(T)_X + \mathbb{V}(T)_Y + \mathbb{W}(T)_Z &= \frac{k_{\mathrm{tN}}}{(\rho c_{\mathrm{P}})_{\mathrm{tN}}}T_{ZZ} + \frac{A_{\mathrm{sr}}Q_{\mathrm{e}}}{(\rho c_{\mathrm{P}})_{\mathrm{tN}}}\exp(-A_{\mathrm{sr}}Z) \\ &+ \frac{Q_{\mathrm{e}}}{(\rho c_{\mathrm{P}})_{\mathrm{tN}}}(T - T_\infty) + \frac{(B_0)^2\sigma_{\mathrm{tN}}(\mathbb{V}^2 + \mathbb{U}^2)}{(\rho c_{\mathrm{P}})_{\mathrm{tN}}[(1 + B_{\mathrm{i}}B_{\mathrm{e}})^2 + (B_{\mathrm{e}})^2]},\end{aligned} \tag{4}$$

$$\begin{aligned}\mathbb{U}(c)_X + \mathbb{V}(c)_Y + \mathbb{W}(c)_Z \\ = D(c)_{ZZ} - k_{\mathrm{e}}\left(\frac{T}{T_0}\right)^n \mathrm{EXP}\left(\frac{-E_0}{k_{\mathrm{b}}T}\right)(c - (c)_\infty).\end{aligned} \tag{5}$$

Boundary conditions [38] in terms of momentum associated with all directions are defined as follows:

$$\left.\begin{aligned}&\mathbb{U} = (Y + X)a, \quad \mathbb{W} = -(a\nu_{\mathrm{Fl}})^{\frac{1}{2}}\int\frac{\mathbb{U}}{\mathrm{aY}}D\eta + z_{\mathbb{W}} \quad \text{at} \\ &X = 0, \quad Z = 0 : \text{as} \quad X = 0, \quad Z \to \infty. \\ &\mathbb{V} = (Y + X)a, \mathbb{W} = (a\nu_{Fl})^{\frac{1}{2}}\int\frac{\mathbb{U}}{aX}D\eta + Z_{\mathbb{W}} : Z = 0, \\ &X = 0 : \mathbb{V} \to 0, \quad X = 0, \quad Z \to \infty.\end{aligned}\right\}. \tag{6}$$

Boundary conditions in terms of concentration, temperature [38]:

$$(T)_\infty \to T, \quad (c)_{\mathbb{W}} = c, \quad (T)_{\mathbb{W}} = T, \quad (c)_\infty \to c. \tag{7}$$

Desired similarity variables [38] are defined as follows:

$$\begin{aligned}\eta = Z\sqrt{\frac{a}{\nu_{\mathrm{Fl}}}}, \quad \mathbb{U} = (Y + X)a\frac{\mathrm{D}F}{\mathrm{D}\eta}, \mathbb{V} = (Y + X)a\frac{\mathrm{D}G}{\mathrm{D}\eta}, \\ w = -(a\nu_{\mathrm{Fl}}(F + G))^{\frac{1}{2}}, \quad F_{\mathbb{W}} = \frac{-z_{\mathbb{W}}}{(a\nu_{\mathrm{Fl}})^{\frac{1}{2}}}, \\ \varphi = \frac{c - (c)_\infty}{(c)_{\mathbb{W}} - (c)_\infty}, \Theta = \frac{T - (T)_\infty}{T_{\mathbb{W}} - (T)_\infty}.\end{aligned} \tag{8}$$

Dimensionless ordinary differential equation (ODEs) are obtained using Eq. (6), which is defined as follows:

$$(1-n)\frac{\mathrm{D}^3F}{\mathrm{d}\eta^3}+n\mathrm{We}\frac{\mathrm{D}^2F}{\mathrm{d}\eta^2}\frac{\mathrm{D}^3F}{\mathrm{d}\eta^3}-\frac{\nu_{\mathrm{Fl}}}{\nu_{\mathrm{tN}}}\left[(F+G)\frac{\mathrm{D}^2F}{\mathrm{d}\eta^2}-\frac{\mathrm{D}F}{\mathrm{d}\eta}\left(\frac{\mathrm{D}F}{\mathrm{d}\eta}+\frac{\mathrm{D}G}{\mathrm{d}\eta}\right)\right]+(F+G)\frac{\mathrm{D}^2F}{\mathrm{d}\eta^2}+\frac{Ha^2}{(1+B_eB_i)^2+(B_e)^2}\left[B_e\frac{\mathrm{D}G}{\mathrm{d}\eta}-(1+B_eB_i)\frac{\mathrm{D}F}{\mathrm{d}\eta}\right]=0, \tag{9}$$

$$(1-n)\frac{\mathrm{D}^3G}{\mathrm{D}\eta^3}+n\mathrm{We}\frac{\mathrm{D}^2G}{\mathrm{D}\eta^2}\frac{\mathrm{D}^3G}{\mathrm{D}\eta^3}-\frac{\nu_{\mathrm{Fl}}}{\nu_{\mathrm{tN}}}\left[(F+G)\frac{\mathrm{D}^2G}{\mathrm{D}\eta^2}-\frac{\mathrm{D}G}{\mathrm{D}\eta}\left(\frac{\mathrm{D}F}{\mathrm{D}\eta}+\frac{\mathrm{D}G}{\mathrm{D}\eta}\right)\right]+(\mathrm{F}+\mathrm{G})\frac{\mathrm{D}^2\mathrm{G}}{\mathrm{D}\eta^2}-\frac{Ha^2}{(1+B_eB_i)^2+(B_e)^2}\left[B_e\frac{\mathrm{D}F}{\mathrm{D}\eta}+(1+B_eB_i)\frac{\mathrm{D}G}{\mathrm{D}\eta}\right]=0, \tag{10}$$

$$\frac{\mathrm{D}^2\Theta}{\mathrm{D}\eta^2}+\frac{(\rho C_{\mathrm{p}})_{\mathrm{Thnf}}k_{\mathrm{Fl}}}{k_{\mathrm{tN}}(\rho C_{\mathrm{p}})_f}\mathrm{Pr}\left[(F+G)\frac{\mathrm{D}\Theta}{\mathrm{D}\eta}-\left(\frac{\mathrm{D}F}{\mathrm{D}\eta}+\frac{\mathrm{D}G}{\mathrm{D}\eta}\right)\Theta\right]-\frac{(\rho C_{\mathrm{p}})_{\mathrm{tN}}k_{\mathrm{Fl}}}{k_{\mathrm{tN}}(\rho C_{\mathrm{p}})_{\mathrm{f}}}\mathrm{Pr}(F+G)\frac{\mathrm{D}\Theta}{\mathrm{D}\eta}+\frac{\mathrm{Pr}\delta Q_{\mathrm{sr}}}{k_{\mathrm{t}}}\exp(-\delta\eta)+\frac{k_{\mathrm{Fl}}}{K_{\mathrm{tN}}}H_{\mathrm{t}}\Theta+\frac{\mathrm{PrEc}Ha^2k_{\mathrm{Fl}}}{k_{\mathrm{tN}}[(1+B_iB_e)^2+(B_e)^2]}\left[\left(\frac{\mathrm{D}F}{\mathrm{D}\eta}\right)^2+\left(\frac{\mathrm{D}G}{\mathrm{D}\eta}\right)^2\right]=0, \tag{11}$$

$$\frac{\mathrm{D}^2\varphi}{\mathrm{D}\eta^2}+\mathrm{Sc}\left[(F+G)\frac{\mathrm{D}\varphi}{\mathrm{D}\eta}-\left(\frac{\mathrm{D}F}{\mathrm{D}\eta}+\frac{\mathrm{D}G}{\mathrm{D}\eta}\right)\varphi\right]-\mathrm{Sc}(F+G)\frac{\mathrm{D}\varphi}{\mathrm{D}\eta}-K_{\mathrm{c}}\mathrm{Sc}(1+\delta\times\Theta)^n\times\exp\left(\frac{-E}{1+\delta^{\times}\Theta}\right)\varphi=0. \tag{12}$$

Boundary conditions for Eqs. (7)–(10) are mentioned [37,38] as follows:

$$\frac{\mathrm{D}F}{\mathrm{D}\eta}(0)=1,\quad \frac{\mathrm{D}G}{\mathrm{D}\eta}(0)=1,\quad F=F_{\mathrm{w}},\Theta(0)=1,\quad \varphi(0)=1,\varphi(\infty)\to 0,\ \Theta(\infty)\to 0,\quad \frac{\mathrm{D}G}{\mathrm{D}\eta}(\infty)\to 0,\ \frac{\mathrm{D}F}{\mathrm{D}\eta}(\infty)\to 0. \tag{13}$$

Correlations associated with tetra-hybrid nanostructures [2] are defined as follows and their values are mentioned in Table 1:

$$\mu_{\mathrm{tN}}=\mu_{\mathrm{Fl}}[(1-\mathrm{O}_4)^{2.5}(1-\mathrm{O}_3)^{2.5}(1-\mathrm{O}_2)^{2.5}(1-\mathrm{O}_1)^{2.5}]^{-1}, \tag{14}$$

Table 1: Thermal characteristics of EO and nanofluid [2]

	k	ρ	ϱ
Al_2O_3	32.9	6,310	5.96×10^{7}
Fe_3O_4	80	5,180	0.112×10^{6}
Cu	401	8,933	59.5×10^{6}
EO	0.144	884	0.125×10^{-11}
TiO_2	8.9538	686.2	4,250

$$\rho_{\mathrm{tN}}=\left[(1-\mathrm{O}_4)\left\{(1-\mathrm{O}_3)(1-\mathrm{O}_2)\left\{\left((1-\mathrm{O}_1)+\frac{\mathrm{O}_1\rho_{\mathrm{sp1}}}{\rho_{\mathrm{Fl}}}\right)\right\}+\frac{\mathrm{O}_2\rho_{\mathrm{sp2}}}{\rho_{\mathrm{Fl}}}+\frac{\mathrm{O}_3\rho_{\mathrm{sp2}}}{\rho_{\mathrm{Fl}}}+\frac{\mathrm{O}_4\rho_{\mathrm{sp2}}}{\rho_{\mathrm{Fl}}}\right\}\right], \tag{15}$$

$$(C_{\mathrm{p}}\rho)_{\mathrm{tN}}=\left[\begin{array}{l}(1-\mathrm{O}_4)(1-\mathrm{O}_3)(1-\mathrm{O}_2)(1-\mathrm{O}_1)\left\{(1-\mathrm{O}_1)\right.\\ \left.+\frac{\mathrm{O}_1(C_{\mathrm{p}}\rho)_{\mathrm{sp1}}}{(C_{\mathrm{p}}\rho)_{\mathrm{Fl}}}\right\}+\frac{\mathrm{O}_2(C_{\mathrm{p}}\rho)_{\mathrm{sp2}}}{(C_{\mathrm{p}}\rho)_{\mathrm{Fl}}}\\ +\frac{\mathrm{O}_3(\rho C_{\mathrm{p}})_{\mathrm{sp3}}}{(\rho C_{\mathrm{p}})_{\mathrm{Fl}}}+\frac{\mathrm{O}_4(C_{\mathrm{p}}\rho)_{\mathrm{sp4}}}{(C_{\mathrm{p}}\rho)_{\mathrm{Fl}}}\end{array}\right], \tag{16}$$

$$\frac{k_{\mathrm{tN}}}{k_{\mathrm{Fl}}}=\frac{(k_{\mathrm{sp4}}+2k_{\mathrm{TR}i}-2\mathrm{O}_4(k_{\mathrm{TR}i}-k_{\mathrm{sp4}}))}{(k_{\mathrm{sp4}}+2k_{\mathrm{TRi}}+\mathrm{O}_4(k_{\mathrm{TRi}}-k_{\mathrm{sp4}}))},\quad \frac{k_{\mathrm{TRi}}}{k_{\mathrm{Fl}}}=\frac{(k_{\mathrm{sp3}}+2k_{\mathrm{hB}}-2\mathrm{O}_3(k_{\mathrm{hB}}-k_{\mathrm{sp3}}))}{(k_{\mathrm{sp3}}+2k_{\mathrm{hB}}+\mathrm{O}_3(k_{\mathrm{hB}}-k_{\mathrm{sp3}}))}, \tag{17}$$

$$\frac{k_{\mathrm{hB}}}{k_{\mathrm{Fl}}}=\frac{(k_{\mathrm{sp2}}+2k_{\mathrm{Nf}}-(2\mathrm{O}_2k_{\mathrm{Nf}}-2\mathrm{O}_2k_{\mathrm{sp2}}))}{(k_{\mathrm{sp2}}+2k_{\mathrm{Nf}}+(\mathrm{O}_2k_{\mathrm{Nf}}-\mathrm{O}_2k_{\mathrm{sp2}}))},\quad \frac{(k_{\mathrm{sp1}}+2k_{\mathrm{f}}-(2\mathrm{O}_1k_{\mathrm{f}}-2\mathrm{O}_1k_{\mathrm{sp1}}))}{(k_{\mathrm{sp1}}+2k_{\mathrm{hB}}+(\mathrm{O}_1k_{\mathrm{f}}-\mathrm{O}_1k_{\mathrm{sp1}}))}=\frac{k_{\mathrm{Nf}}}{k_{\mathrm{f}}}, \tag{18}$$

$$\frac{\varrho_{\mathrm{tN}}}{\varrho_{\mathrm{Fl}}}=\frac{(\varrho_{\mathrm{sp4}}+2\varrho_{\mathrm{TRi}}-2(\mathrm{O}_4\varrho_{\mathrm{TRi}}-\mathrm{O}_4\varrho_{\mathrm{sp4}}))}{(\varrho_{sp4}+2\varrho_{\mathrm{TRi}}+2(\mathrm{O}_4\varrho_{\mathrm{TRi}}-\mathrm{O}_4\varrho_{\mathrm{sp4}}))},\quad \frac{(\varrho_{\mathrm{sp3}}+2\varrho_{\mathrm{hB}}-2(\mathrm{O}_3\varrho_{\mathrm{hB}}-\mathrm{O}_3\varrho_{\mathrm{sp3}}))}{(\varrho_{\mathrm{sp3}}+2\varrho_{\mathrm{hB}}+2(\mathrm{O}_3\varrho_{\mathrm{hB}}-\mathrm{O}_3\varrho_{\mathrm{sp3}}))}=\frac{\varrho_{\mathrm{TRi}}}{\varrho_{\mathrm{Fl}}}, \tag{19}$$

$$\frac{\varrho_{\mathrm{hB}}}{\varrho_{\mathrm{Fl}}}=\frac{(\varrho_{\mathrm{sp2}}+2\varrho_{\mathrm{Nf}}-2(\mathrm{O}_2\varrho_{\mathrm{Nf}}-\mathrm{O}_2\varrho_{\mathrm{sp2}}))}{(\varrho_{\mathrm{sp2}}+2\varrho_{\mathrm{Nf}}+2(\mathrm{O}_2\varrho_{\mathrm{Nf}}-\mathrm{O}_2\varrho_{\mathrm{sp2}}))},\quad \frac{(\varrho_{\mathrm{sp1}}+2\varrho_{\mathrm{f}}-2(\mathrm{O}_1\varrho_{\mathrm{f}}-\mathrm{O}_1\varrho_{\mathrm{sp1}}))}{(\varrho_{\mathrm{sp1}}+2\varrho_{\mathrm{f}}+2(\mathrm{O}_1\varrho_{\mathrm{f}}-\mathrm{O}_1\varrho_{\mathrm{sp1}}))}=\frac{\varrho_{\mathrm{Nf}}}{\varrho_{\mathrm{Fl}}}, \tag{20}$$

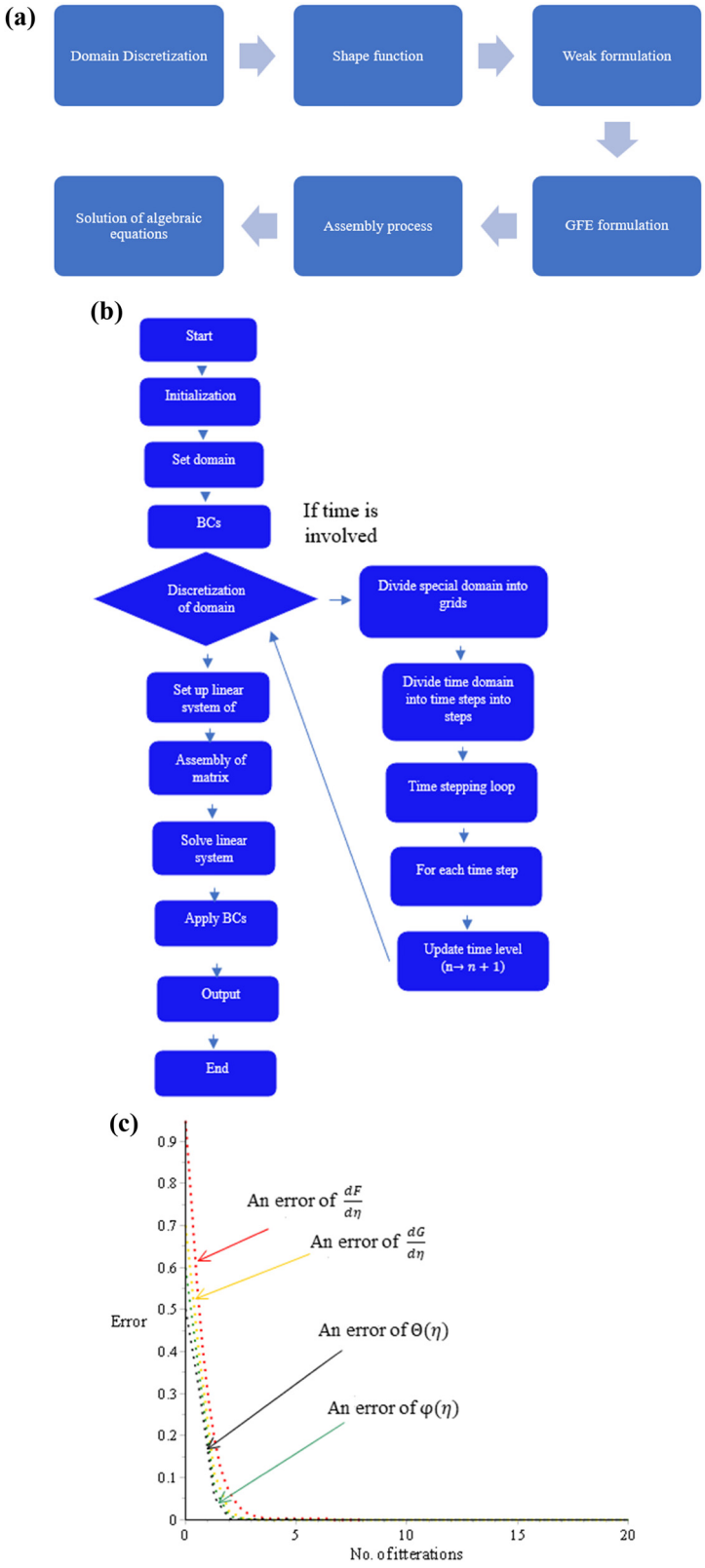

Figure 2: (a) Basic steps related to GFEA. (b) Flowchart of the numerical approach. (c) An error analysis *versus* number of iterations.

Table 2: Grid sizes analysis of concentration, velocity, and temperature profile against different number of elements [37]

e	$\frac{\mathrm{D}F}{\mathrm{D}\eta}\left(\frac{\eta_{\max}}{2}\right)$	$\frac{\mathrm{D}G}{\mathrm{D}\eta}\left(\frac{\eta_{\max}}{2}\right)$	$\Theta\left(\frac{\eta_{\max}}{2}\right)$	$\varphi\left(\frac{\eta_{\max}}{2}\right)$
30	0.8384270445	0.08661484179	0.01744270380	0.5114785103
60	0.7515563525	0.06908386806	0.01907272568	0.4152217411
90	0.7230934157	0.06394110550	0.01932808058	0.4896739344
120	0.7089885500	0.06149219508	0.01941012442	0.4869869959
150	0.7005771653	0.06006088523	0.01944573501	0.4853785126
180	0.6949876348	0.05912224772	0.01946401568	0.4843078233
210	0.6910074217	0.05845934598	0.01947447561	0.4835437149
240	0.6880267209	0.05796629441	0.01948094416	0.4829710196
270	0.6857129928	0.05758514901	0.01948510176	0.4825257083
300	0.6838632604	0.05728180477	0.01948796720	0.4821698251

$$\frac{k_{\mathrm{tN}}}{k_{\mathrm{Fl}}} = \left[\begin{array}{l} \dfrac{(k_{\mathrm{sp4}} + 2k_{\mathrm{TRi}} - 2(\mathrm{O}_4k_{\mathrm{TRi}} - \mathrm{O}_4k_{\mathrm{sp4}}))}{(k_{\mathrm{sp4}} + 2k_{\mathrm{TRi}} + (\mathrm{O}_4k_{\mathrm{TRi}} - \mathrm{O}_4k_{\mathrm{sp4}}))} \\ \quad \times \dfrac{(k_{\mathrm{sp3}} + 2k_{\mathrm{hB}} - 2(\mathrm{O}_3k_{\mathrm{hB}} - \mathrm{O}_3k_{\mathrm{sp3}}))}{(k_{\mathrm{sp3}} + 2k_{\mathrm{hB}} + (\mathrm{O}_3k_{\mathrm{hB}} - \mathrm{O}_3k_{\mathrm{sp3}}))} \\ \dfrac{(k_{\mathrm{sp2}} + 2k_{\mathrm{hB}} - 2(\mathrm{O}_2k_{\mathrm{Nf}} - \mathrm{O}_2k_{\mathrm{sp2}}))}{(k_{\mathrm{sp2}} + 2k_{\mathrm{hB}} + (\mathrm{O}_2k_{\mathrm{hB}} - \mathrm{O}_2k_{\mathrm{sp2}}))} \\ \quad \times \dfrac{(k_{\mathrm{sp1}} + 2k_{\mathrm{f}} - 2(\mathrm{O}_1k_{\mathrm{Nf}} - \mathrm{O}_1k_{\mathrm{sp1}}))}{(k_{\mathrm{sp1}} + 2k_{\mathrm{f}} + (\mathrm{O}_1k_{\mathrm{f}} - \mathrm{O}_1k_{\mathrm{sp1}}))} \end{array}\right], \tag{21}$$

$$\frac{\varrho_{\mathrm{tN}}}{\varrho_{\mathrm{f}}} = \left[\begin{array}{l} \dfrac{(\varrho_{\mathrm{sp4}} + 2\varrho_{\mathrm{TRi}} - 2(\mathrm{O}_4\varrho_{\mathrm{TRi}} - \mathrm{O}_4\varrho_{\mathrm{sp4}}))}{(\varrho_{\mathrm{sp3}} + 2\varrho_{\mathrm{TRi}} + (\mathrm{O}_4\varrho_{\mathrm{TRi}} - \mathrm{O}_4\varrho_{\mathrm{sp4}}))} \\ \quad \times \dfrac{(\varrho_{\mathrm{sp3}} + 2\varrho_{\mathrm{hB}} - 2(\mathrm{O}_3\varrho_{\mathrm{hB}} - \mathrm{O}_3\varrho_{\mathrm{sp3}}))}{(\varrho_{\mathrm{sp3}} + 2\varrho_{\mathrm{hB}} + (\mathrm{O}_3\varrho_{\mathrm{hB}} - \mathrm{O}_3\varrho_{\mathrm{sp3}}))} \\ \dfrac{(\varrho_{\mathrm{sp2}} + 2\varrho_{\mathrm{Nf}} - 2(\mathrm{O}_2\varrho_{\mathrm{Nf}} - \mathrm{O}_2\varrho_{\mathrm{sp3}}))}{(\varrho_{\mathrm{sp3}} + 2\varrho_{\mathrm{Nf}} + (\mathrm{O}_3\varrho_{\mathrm{Nf}} - \mathrm{O}_3\varrho_{\mathrm{sp3}}))} \\ \quad \times \dfrac{(\varrho_{\mathrm{sp1}} + 2\varrho_{\mathrm{f}} - 2\mathrm{O}_1(\varrho_{\mathrm{f}} - \varrho_{\mathrm{sp1}}))}{(\varrho_{\mathrm{sp1}} + 2\varrho_{\mathrm{f}} + (\mathrm{O}_1\varrho_{\mathrm{f}} - \mathrm{O}_1\varrho_{\mathrm{sp1}}))} \end{array}\right]. \tag{22}$$

Skin friction factors in terms of y- and x-directions [38] are represented as follows:

$$\begin{aligned} c_{\mathrm{Fx}} &= \frac{\tau_{ZX}\,|_{Z=0}}{\rho_{\mathrm{tN}}(\mathbb{U}_{\mathrm{w}})^2}, \quad c_{\mathrm{FX}}(\mathrm{Re})^{-\frac{1}{2}} \\ &= \frac{\left[(1-n)\frac{\mathrm{D}^2F}{\mathrm{D}\eta^2}(0) + \frac{n}{2}\mathrm{We}\left(\frac{\mathrm{D}^2F}{\mathrm{D}\eta^2}(0)\right)^2\right]}{(1-\mathrm{O}_4)^{2.5}(1-\mathrm{O}_3)^{2.5}(1-\mathrm{O}_2)^{2.5}(1-\mathrm{O}_1)^{2.5}}, \end{aligned} \tag{23}$$

$$\begin{aligned} c_{\mathrm{GY}} &= \frac{\tau_{ZY}\,|_{Z=0}}{\rho_{\mathrm{tN}}(\mathbb{V}_{\mathrm{w}})^2}, \quad c_{\mathrm{GY}}(\mathrm{Re})^{-\frac{1}{2}} \\ &= \frac{\left[(1-n)\frac{\mathrm{D}^2G}{\mathrm{D}\eta^2}(0) + \frac{n}{2}\mathrm{We}\left(\frac{\mathrm{D}^2G}{\mathrm{D}\eta^2}(0)\right)^2\right]}{(1-\mathrm{O}_4)^{2.5}(1-\mathrm{O}_3)^{2.5}(1-\mathrm{O}_2)^{2.5}(1-\mathrm{O}_1)^{2.5}}. \end{aligned} \tag{24}$$

Heat transfer and mass diffusion rates in normal form [38] are predicted as follows:

$$\mathrm{Nu}(\mathrm{Re})^{-\frac{1}{2}} = -\frac{K_{\mathrm{tN}}}{K_{\mathrm{Fl}}}\frac{\mathrm{D}\Theta}{\mathrm{D}\eta}(0), \tag{25}$$

$$\mathrm{Sh}(\mathrm{Re})^{-\frac{1}{2}} = -\frac{\mathrm{D}\varphi}{\mathrm{D}\eta}(0). \tag{26}$$

3 Numerical methodology

Galerkin finite element approach (GFEA) [39,40] is visualized as a powerful tool for obtaining numerical solutions of complex nonlinear ODEs utilized in physics and engineering fields. GFEA provides an effective way and accurate way for approximate solution of complex ODEs. The basic steps of GFEA are listed below. The steps of finite element method (FEM) are addressed in Figure 2a. FEM's advantages are mentioned as FEM deals with complex problems and with various kinds of boundary conditions. FEM needs less investment in case of resources and time. For a variety of physical models arising in applied sciences, this approach is the most appropriate one. FEM is very good at

Table 3: Comparison results of $\Theta'(0)$ with the published study [38] for limiting case

Pr	Bilal *et al.* [38]	Present study
0.07	0.0656	0.065613701
0.2	0.1691	0.169180630
0.7	0.4539	0.453014010
2	0.9144	0.914440103
7	1.8953	1.895110832

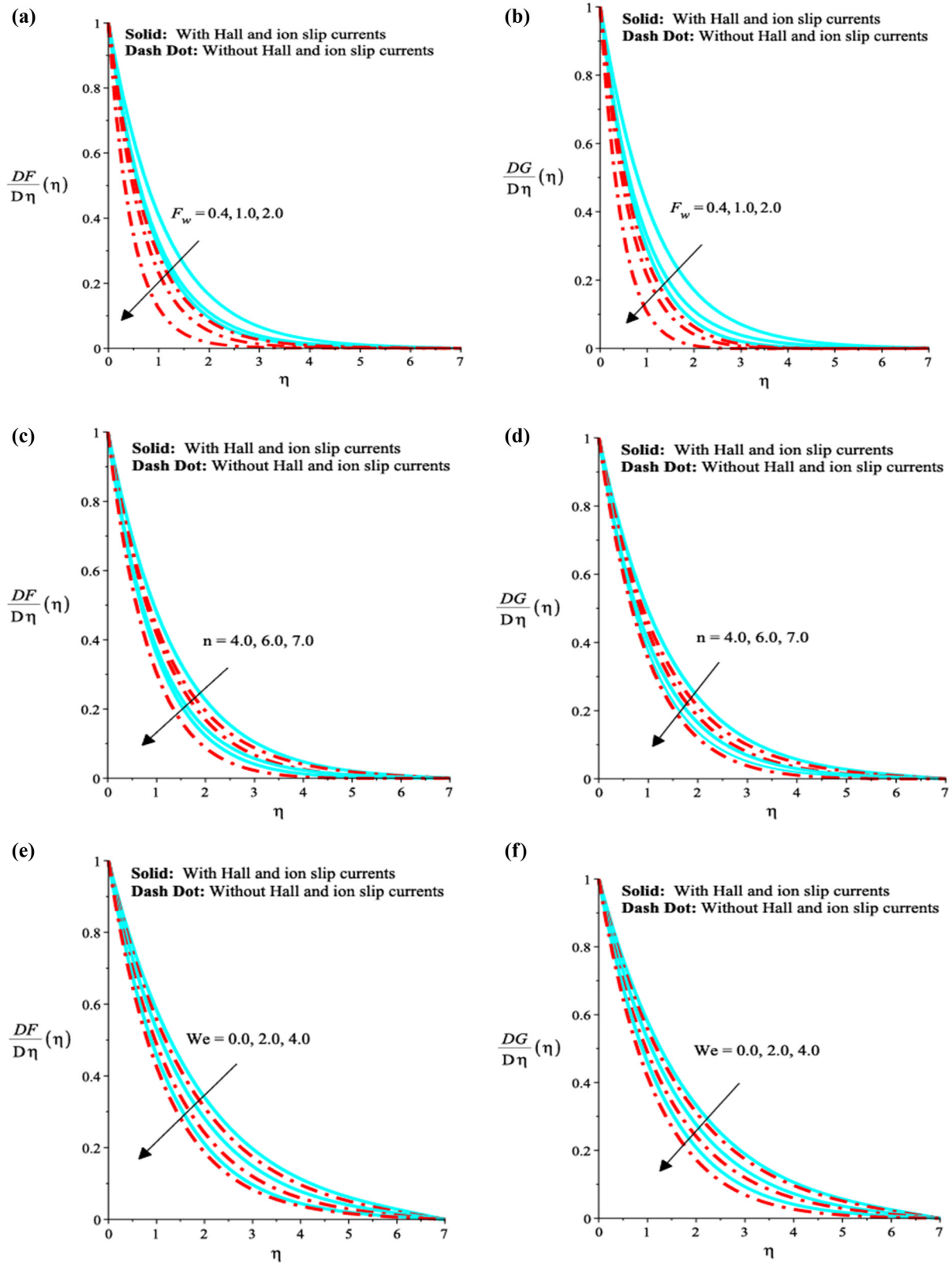

Figure 3: (a) Various values of F_w on $\frac{DF}{D\eta}$. (b) Various values of F_w on $\frac{DG}{D\eta}$. (c) Various values of n on $\frac{DF}{D\eta}$. (d) Various values of n on $\frac{DG}{D\eta}$. (e). Various values of We on $\frac{DF}{D\eta}$. (f) Various values of We on $\frac{DG}{D\eta}$. (g) Various values of B_i on $\frac{DF}{D\eta}$. (h) Various values of B_i on $\frac{DG}{D\eta}$. (i) Various values of B_e on $\frac{DF}{D\eta}$. (j) Various values of B_e on $\frac{DG}{D\eta}$.

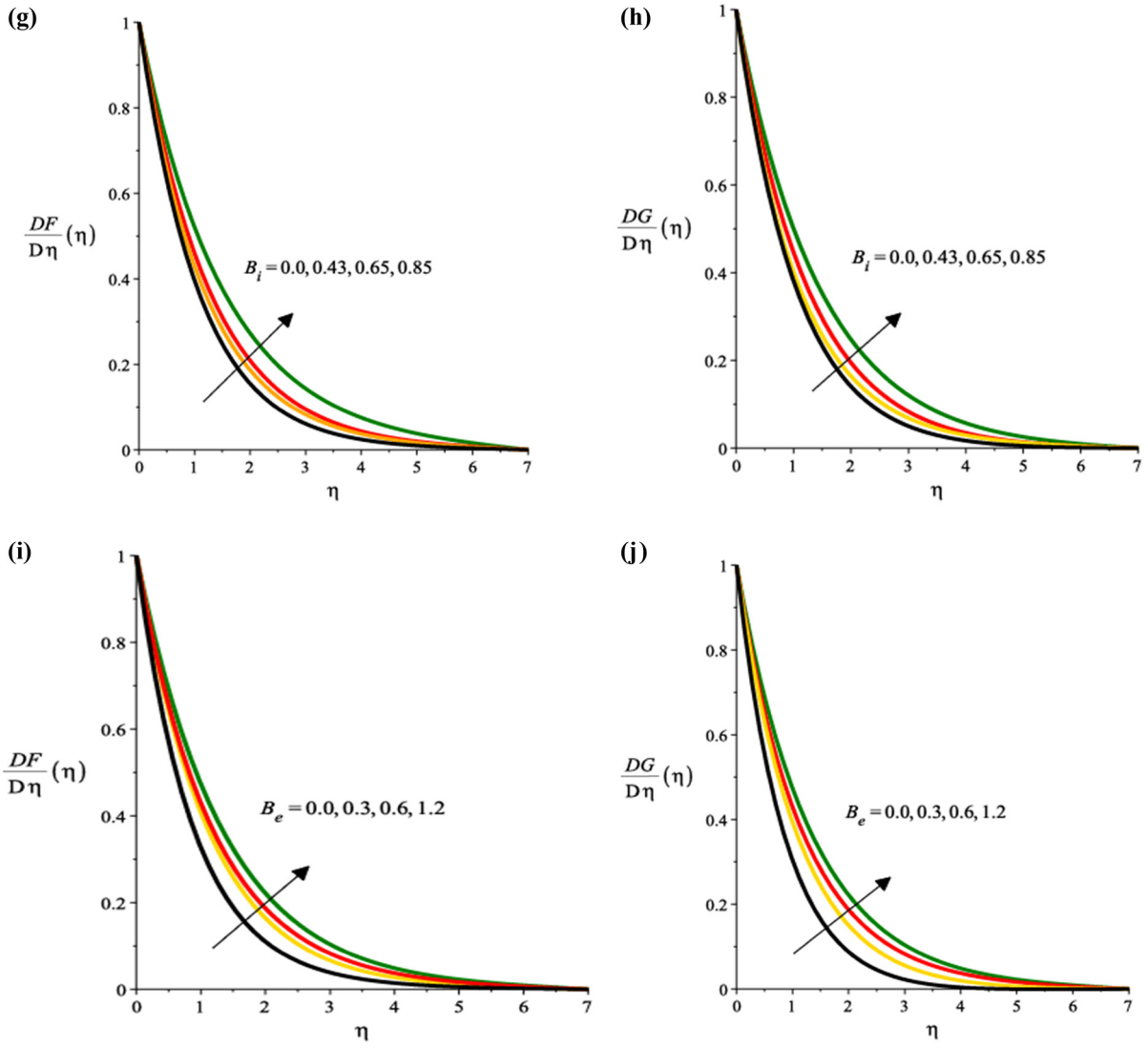

Figure 3: (*Continued*)

dealing with derivatives' discretization. Using numerical simulations, FEM enables the validation of theoretical models and hypotheses.

Step 1: Discretization's

Dividing the problem domain into smaller components, or elements is the first step. Using up to 300 elements is found to be adequate for simulating the current analysis's solution. The system of ODEs is represented by the "strong form," and the "weak form" is produced using a process known as the residual method.

Step 2: Shape functions

In the current analysis, linear shape functions are utilized as essential for approximating solutions. These functions help for obtaining solutions. Although the finite element method uses a variety of shape function types, linear shape functions are used in this analysis. These linear shape functions accurately capture the fundamental behavior of the system while streamlining the approximation process.

Step 3: Weak formulation

Boundary conditions and strong form are associated with Eqs. (12)–(14). Weak forms are required in this process to obtain an approximate solution. All terms are gathered on one side and integrated with more than 300 elements. Grid independent survey is shown in Table 2.

Step 4: Finite element formulation

The current problem's stiffness elements are obtained in this step. Global stiffness matrices are attained for every element in the end.

Step 5: Assembly process

A crucial component of the finite element method is the assembly process. The assemblage concept is used to formulate stiffness matrices.

Step 6: Solution of algebraic equations

Finally, a numerical solution within 10^{-5} computational tolerance is obtained for the system of linear algebraic equations. The following is a list of the stopping conditions [37]. The flow chart of the current approach is illustrated in Figure 2b.

$$\left|\frac{\aleph_{i+1} - \aleph_i}{\aleph^i}\right| < 10^{-5}. \tag{27}$$

Here, i is the number of iterations and $\aleph$ is nodal values. An error analysis of $\frac{dG}{d\eta}$, $\frac{dF}{d\eta}$, $\Theta(\eta)$, and $\varphi(\eta)$ is plotted in Figure 2c *versus* several iterations. It noticed that the error of $\frac{dG}{d\eta}$, $\frac{dF}{d\eta}$, $\Theta(\eta)$, and $\varphi(\eta)$ is decreased when several iterations are enhanced. By increasing values of iterations, error plots of $\frac{dG}{d\eta}$, $\frac{dF}{d\eta}$, $\Theta(\eta)$, and $\varphi(\eta)$ are decreased. Table 3 exhibits validation of the current study with the study [38]. The values of $-\Theta'(0)$ are recorded in Table 3 with the change of Pr.

4 Results and discussion

Concentration and thermal features in a complex fluid using charged particles and tetra-hybrid nanoparticles are considered toward a 3D surface. Solar thermal radiation and activation are addressed in the energy equation as well as the concentration equation. Such complex modeling is tackled numerically by using a finite element approach. Detailed discussions are mentioned below.

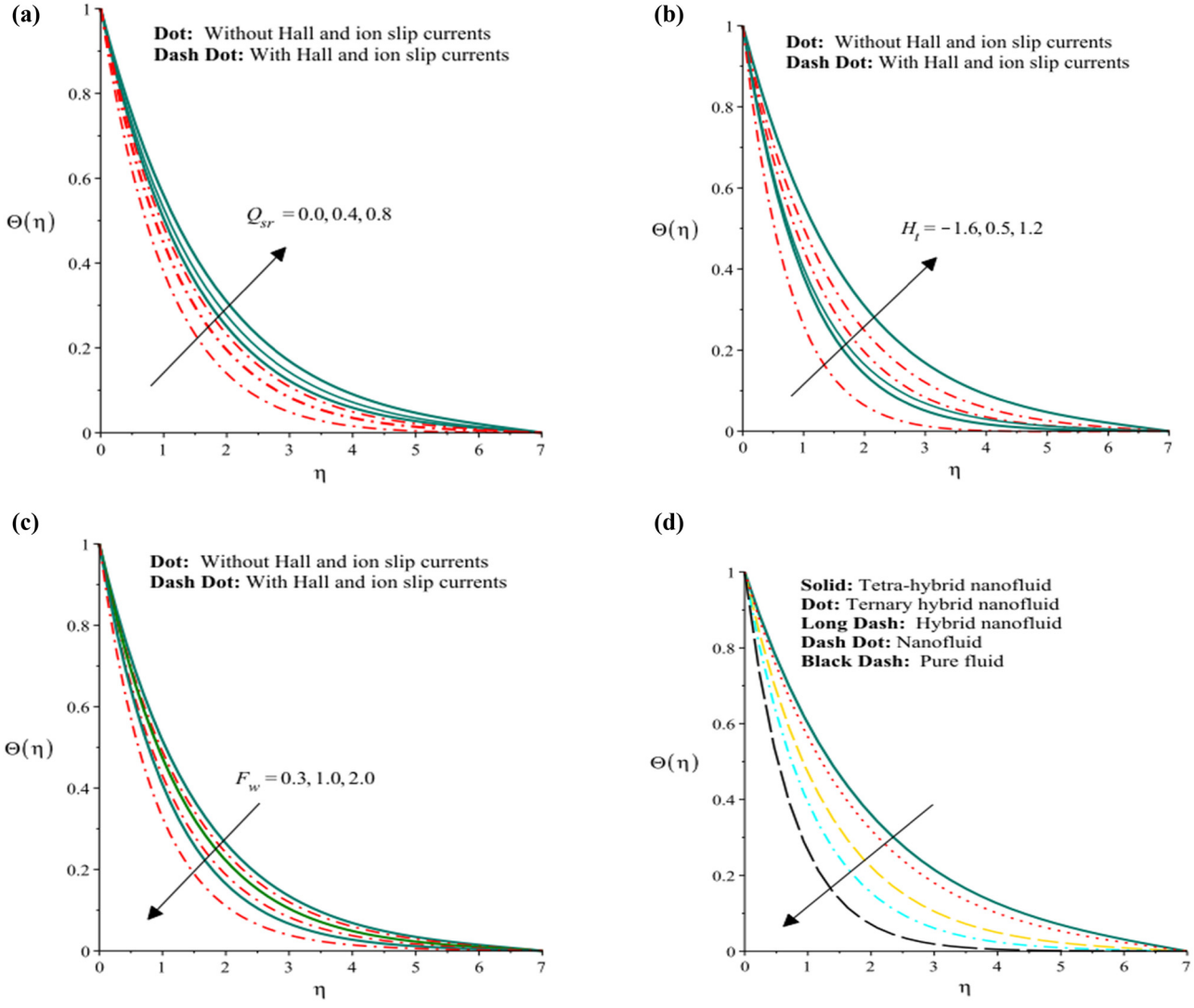

Figure 4: (a) Various values of Q_{sr} on $\Theta(\eta)$. (b) Various values of H_t on $\Theta(\eta)$. (c) Various values of F_w on $\Theta(\eta)$. (d) Comparative analysis between several nanofluids.

Figure 3a–j reveal influences of F_w, c, We, B_i, and B_e on y- and x-components of velocity. Solid curves on graphs are plotted using influence of the role on B_i and B_e, while dash-dot curves on the graphs are without impact of B_i and B_e. It was experienced that the motion is induced by the presence of charged particles (ion slip and Hall currents) is higher than the force induced without impacts of ion slip and Hall forces. Figure 3a and b signify the role of F_w with velocity curves (both directions). It was observed that motion associated with nanoparticles is declined when F_w is enhanced. The role of power law index parameter with velocity curves is addressed in Figure 3c and d using charged particles. In Figure 3c and d, motion of charged particles along with tetra-hybrid nanoparticles is slow down. The description of the non-Newtonian behavior of some fluids, including polymers, suspensions, and slurries, is the power law index, also known as the flow behavior index. The fluid's viscosity is a function of the shear rate, or the rate at which it deforms as a result of an applied force, and is called n. Increasing the power law index causes the fluid to become more shear-thickening, which causes its viscosity to rise as the shear rate rises. Because of the higher viscosity, if the fluid is moving through a pipe or a channel, the velocity of the fluid will drop. Figure 3e and f shows influences of Weissenberg number (We) on both components regarding the velocity field using the concept of charged particles. A decreasing function is predicted among velocity field and Weissenberg number. A dimensionless quantity is known as the We describe the elasticity of several fluids, including melts and solutions of polymers. The proportion of elastic to viscous forces in a fluid is expressed by the Weissenberg number. The fluid becomes more elastic as the Weissenberg number rises, which can have a major impact on the fluid's velocity field.

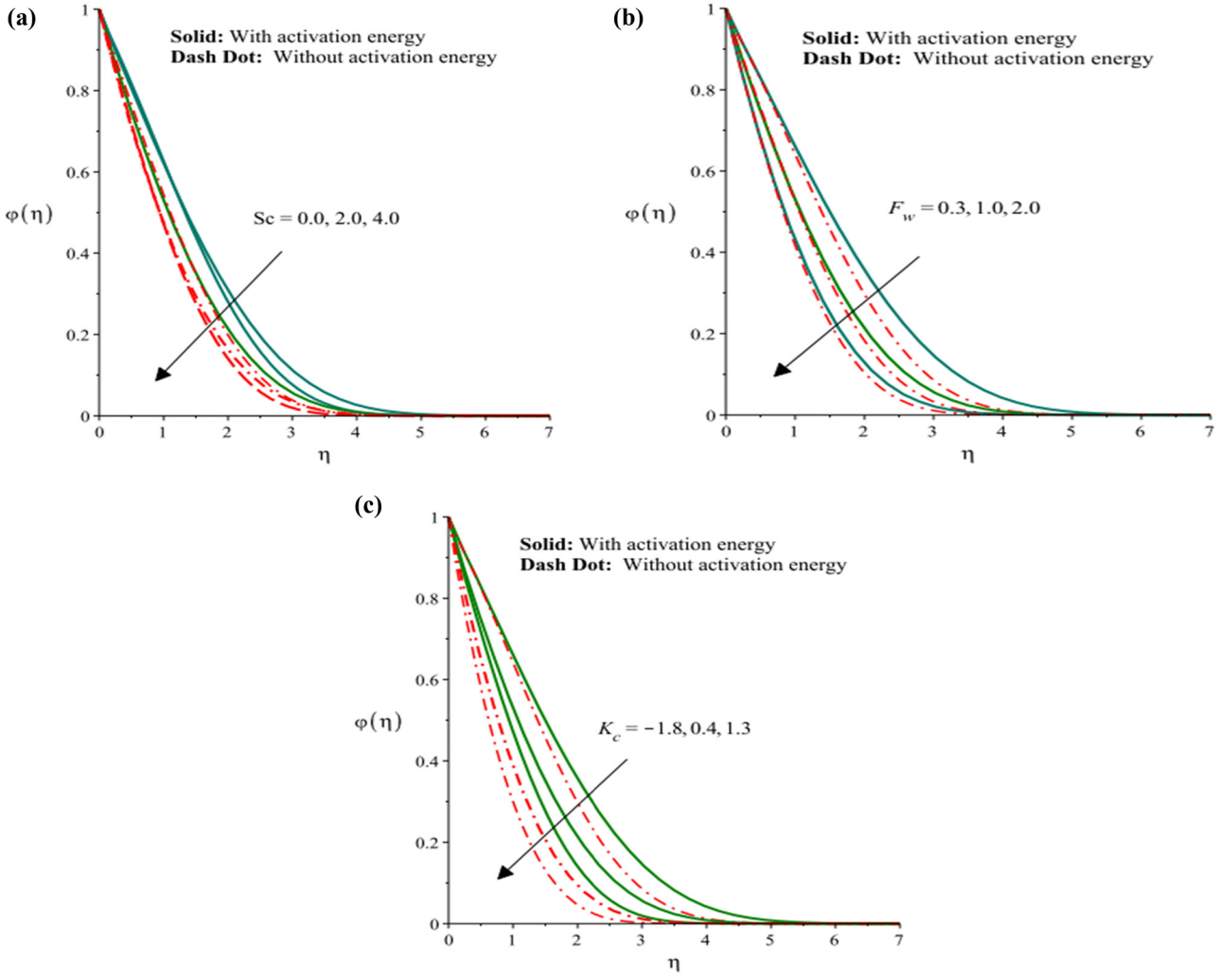

Figure 5: (a) Various values of Sc on $\varphi(\eta)$. (b) Various values of F_w on $\varphi(\eta)$. (c) Various values of K_c on $\varphi(\eta)$.

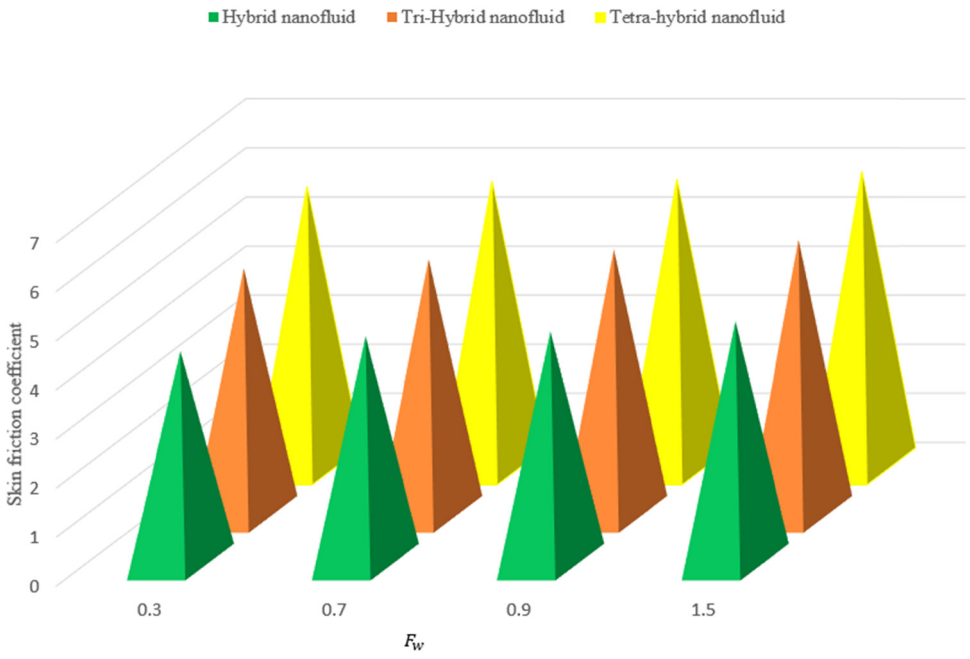

Figure 6: Various values of F_w on divergent velocity with different nanoparticles.

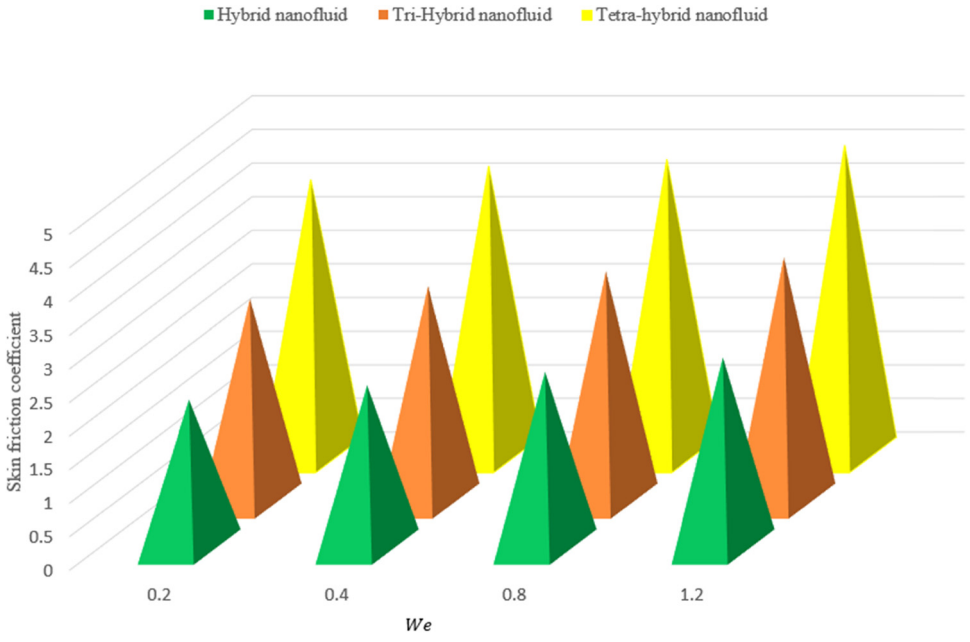

Figure 7: Various values of We on the divergent velocity with different nanoparticles.

Figure 3g and h reveals the role of B_i on both components of velocity fields. Here, B_i is known as the ion slip parameter. B_i is a dimensionless number that describes how important electrical and viscous forces are about one another in a fluid. The ratio of the fluid velocity to the ion drift velocity is described by B_i. The ions take on a greater role in directing the fluid flow as B_i rises. Through collisions, the ions impart momentum to the fluid, with faster-moving ions imparting greater momentum than slower-moving ions. The fluid velocity may rise as a result of this accelerated momentum transfer. Figure 3i and j reveals impact of Hall parameter on both components of velocity fields. Velocity fields increase when the ion slip parameter is enhanced. The Hall current, which propels

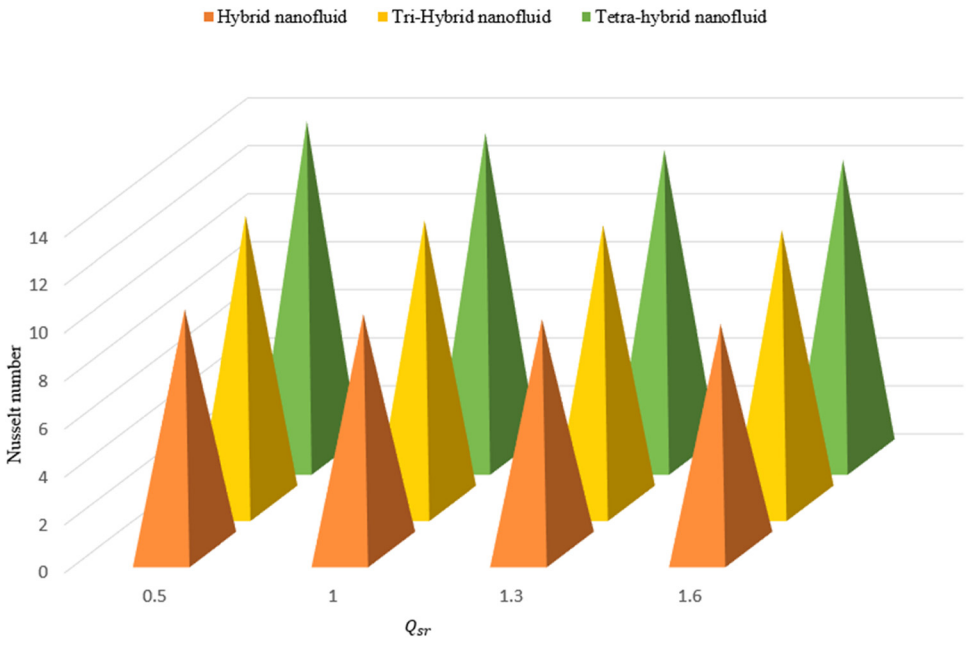

Figure 8: Various values of Q_{sr} on Nusselt number with different nanoparticles.

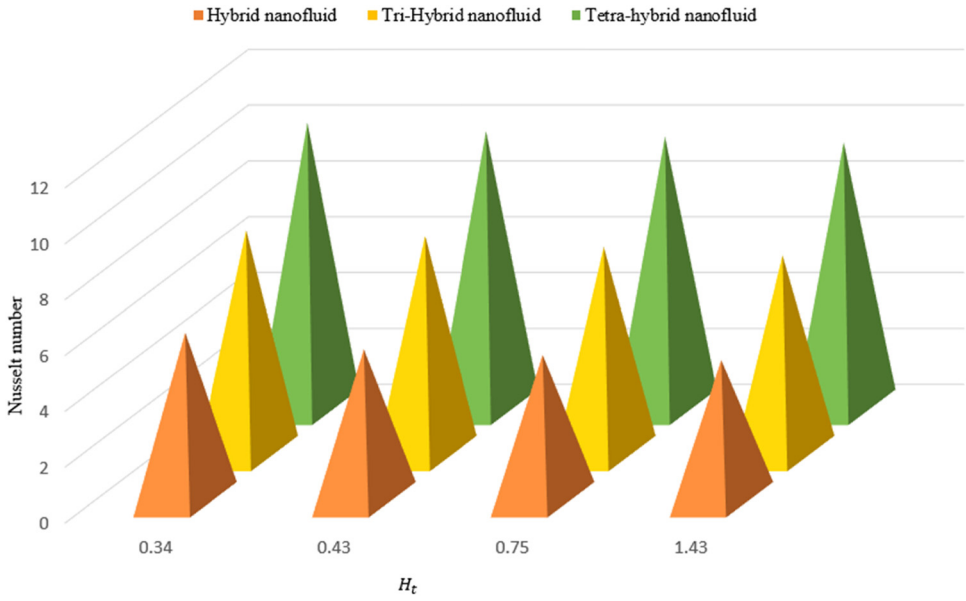

Figure 9: Various values of H_t on Nusselt number with different nanoparticles.

a flow of charged particles in a direction perpendicular to both magnetohydrodynamic and electric field, is what causes the velocity field to grow when B_e is increased. The Hall effect can also result in the development of plasma vortices or other instability, which can improve the velocity field of the plasma.

Figure 4a–c shows the roles of (Q_{sr}), heat source number (H_t), and suction parameter on temperature profile in the presence of charged particles. Figure 4a–c reveals comparative among charged particles. Figure 4a demonstrates visualization of solar thermal radiation on temperature profile. Heat energy inclines due to the enhancement of solar thermal radiation (Q_{sr}). The increasing absorption of solar radiation is one physical factor contributing to the temperature field's rise when the solar thermal radiation number rises. The thermal role of charged particles is then thermal performance for the absence

Table 4: Comparative simulations of thermal performance of between Al_2O_3–Fe_3O_4–Cu–TiO_2/SA and Al_2O_3–Fe_3O_4–Cu/EO on Nusselt number with variation of We, c, F_w, Q_{sr}, and Ha

					Al_2O_3–Fe_3O_4–Cu–TiO_2/SA		Al_2O_3–Fe_3O_4–Cu/EO	
We	c	F_w	Q_{sr}	**Ha**	$-c_{FX}(\mathrm{Re})^{-1/2}$	$-c_{GY}(\mathrm{Re})^{-1/2}$	$-c_{FX}(\mathrm{Re})^{-1/2}$	$-c_{GY}(\mathrm{Re})^{-1/2}$
0.0	0.5	0.4	1.4	1.5	0.02214343196	0.05865898871	0.07266287156	0.12135323323
2.0					0.03587113453	0.04246094407	0.08724670203	0.26330664027
4.0					0.05236673372	0.03326979664	0.09810657859	0.34797443923
	2.0				0.00950051048	0.02598226450	0.02256750403	0.03861635206
	4.0				0.01264731771	0.03397385437	0.03885189101	0.07231154774
	6.0				0.04372798391	0.03680292477	0.05059515494	0.08727917314
		0.0			0.01856543134	0.04129726496	0.01273542769	0.03030398189
		1.3			0.02423938981	0.04202520257	0.05428624517	0.04183968540
		2.0			0.02672351517	0.04537765340	0.07672696670	0.05293624497
			0.2		0.32243788869	0.04446320779	0.05375377186	0.05956787390
			0.8		0.11033100431	0.03121021812	0.04595902956	0.03616076937
			1.2		0.13130821421	0.02012330113	0.03672696670	0.01293624497
				0.0	0.02253932893	0.03864942556	0.00581049307	0.01289901734
				0.4	0.03120201832	0.04123101423	0.04002619772	0.02047166234
				0.8	0.04037012420	0.04560190320	0.05091923911	0.05209635957

of charged particles. Figure 4b predicts the behavior of thermal energy against heat source number (H_t). The heat source number (H_t), a dimensionless metric, expresses how important heat creation is about conductive heat transport. The ratio of the heat generation rate to the conductive heat transfer rate is indicated by the heat source number. As the number of heat sources rises, the amount of heat generation contributing to overall heat transfer increases, which can have a major impact on the temperature field. The increase in the quantity of heat produced per unit volume is one physical factor contributing to the temperature field's rise as the number of heat sources rises. Figure 4c presents the contribution of (F_w) on fluid temperature. Comparative analysis between multiple nanofluids is addressed in Figure 4d. Here, solid curves on the graphs are plotted for visualization of tN, dot curves are due to TRi, hybrid nanofluids are revealed by long dash curves, nanofluids are due to dash dot curves, and pure fluid is shown by black dash curves. Maximum production has been achieved for tN rather than for TRi nanoparticles, hybrid nanofluid, and nanofluid and working fluid.

Figure 5a–c plots the experience of Sc, F_w, and K_c on mass diffusion with activation energy and without activation energy. Figure 5a estimates the behavior of the Schmidt number (Sc) on the mass diffusion profile in the presence of activation energy and absence of activation energy. The relative significance of mass diffusion and momentum diffusion in a fluid is expressed by the dimensionless Schmidt number (Sc). $\mathrm{Sc} = \nu/D$, where ν is the kinematic viscosity and D is the diffusion coefficient, is the ratio of the fluid's viscosity to the sum of its density and diffusion coefficient. When the Schmidt number rises, it indicates that the fluid's diffusion coefficient is relatively low when compared to its viscosity. For instance, when the fluid is extremely viscous or when the diffusing species is particularly big or heavy, this may occur. When this occurs, the rate of mass diffusion is decreased because the molecules or particles that are diffusing face more movement resistance as a result of the viscous forces of fluid. Figure 5b captures the experience of the suction number on the mass diffusion profile. In Figure 5b, mass diffusion declines when the suction parameter is enhanced. The role of chemical reaction number on mass diffusion is carried out in Figure 5c. The characteristic time scale of the chemical reaction is substantially shorter than the characteristic time scale of mass diffusion when the number of chemical reactions increases. This may occur, for instance, when the reaction rate is rapid or when the species that is diffusing the energy is highly reactive. As a result of the chemical reaction's quick consumption or production of the diffusing species, the concentration gradient in these situations is minimized, which lowers the rate of mass diffusion. Figures 6 and 7 show the estimation of the suction number (F_w) and the Weissenberg number (We) on skin friction coefficients. It was observed that the skin friction coefficient increases when F_w is increased. The similar behavior is estimated on skin friction coefficient *versus* enhancement of Weissenberg number (We). Figures 8 and 9 demonstrate the impacts of Q_{sr} and H_t on the Nusselt number including suspensions of nanoparticles. Nusselt number declines when Q_{sr} and H_t are increased. Moreover, maximum thermal enhancement for tetra-hybrid nanofluid rather than nanofluid, tri-hybrid nanofluid and nanofluid in

view of skin friction coefficient and Nusselt number. Table 3 presents the comparative study of the present finding with the published data. Table 4 reveals observations of We, n, F_w, Q_{sr}, and H_t on Nusselt number. It was included that maximum enactment for heat energy has been investigated for Al_2O_3–Fe_3O_4–Cu–TiO_2/SA rather than thermal performance for Al_2O_3–Fe_3O_4–Cu/SA.

5 Conclusions

Multiple features of activation energy and solar thermal radiations past the 3D surface including various types of nanoparticles are addressed here. Charged particles with EO are inserted in the complex fluid. The present complex model is tacked numerically by finite element methodology. Convergence of required problem is ensured in view of Table 2. Concluding remarks of the present model are mentioned as when there are charged particles present, there is more motion and thermal energy than when there are no charged particles present. Mass diffusion in the presence of activation energy is higher than mass diffusion in the absence of activation energy. Maximum cooling process and maximum thermal energy for case tetra-hybrid nanofluid rather than tri-hybrid nanoparticles and nanofluid. With the enhancement of charged particles, motion regarding nanoparticles is enhanced *versus* enhancement of charged particles. The greater the power law index, suction, and Weissenberg number, the acceleration of nanoparticles is enhanced. The highest thermal energy is achieved *versus* enhancement of solar thermal radiation and heat sink number, but minimum thermal energy can be achieved when the suction number is increased. Mass diffusion decreases against inclination Schmidt number, suction, and chemical reaction numbers. In residential, commercial, and industrial facilities, solar thermal radiation may be employed to warm water. In distant areas without electricity, refrigeration systems can be powered by solar thermal radiation and utilized to keep food and other perishable products.

6 Future directions

The current model is associated with tangent hyperbolic liquid addition of nanofluids on a 3D surface. Further, the forces of ion slip and Hall currents are observed. Utilizations of FEM for numerical procedure and graphical outcomes are observed. In the future, the current model will be studied using complex rhetorical fluids like Bingham plastic, Herschel-Bulkley, and third and fourth-grade fluids employing a finite element approach. Moreover, the current model with Bingham plastic, Herschel-Bulkley, and third- and fourth-grade fluids in the form of partial differential equations will be simulated with FEM. In the future, new correlations of hybrid nanofluid will be implemented for measuring thermal efficiency.

Acknowledgments: The author Thabet Abdeljawad would like to thank Prince Sultan University for paying the support through the TAS research lab.

Funding information: This work was partially supported by the University Natural Science Research Project of Anhui Province (Project No. 2023AH050314) and the Horizontal Scientific Research Funds in Huaibei Normal University (No. 2024340603000006).

Author contributions: All authors have accepted responsibility for the entire content of this manuscript and approved its submission.

Conflict of interest: The authors state no conflict of interest.

Data availability statement: The datasets generated and/or analysed during the current study are available from the corresponding author on reasonable request.

References

[1] Jamshed W, Eid MR, Nisar KS, Nasir NAAM, Edacherian A, Saleel CA, et al. A numerical frame work of magnetically driven Powell-Eyring nanofluid using single phase model. Sci Rep. 2021;11(1):1–26.

[2] Sohail M, Nazir U, Singh A, Tulu A, Khan MJ. Finite element analysis of cross fluid model over a vertical disk suspended to a tetra hybrid nanoparticles mixture. Sci Rep. 2024;14(1):1–17.

[3] Waseem F, Sohail M, Ilyas N, Awwad EM, Sharaf M, Khan MJ, et al. Entropy analysis of MHD hybrid nanoparticles with OHAM considering viscous dissipation and thermal radiation. Sci Rep. 2024;14(1):1096.

[4] Waseem F, Sohail M, Singh A. Entropy analysis of three-dimensional stretched magnetized hybrid nanofluid with thermal radiation and heat generation. BioNanoScience. 2023;1–19.

[5] Li S, Sohail M, Nazir U, Sherif E, Hassan A. Statistical investigations and morphological aspects of cross-rheological material suspended in transportation of alumina, silica, titanium, and ethylene glycol *via* the Galerkin algorithm. Nanotechnol Rev. 2023;12(Issue 1):20230169.

[6] Aziz A, Jamshed W, Aziz T, Bahaidarah HM, Rehman KU. Entropy analysis of Powell–Eyring hybrid nanofluid including effect of linear thermal radiation and viscous dissipation. J Therm Anal Calorim. 2021;143(2):1331–43.

[7] Jamshed W, Al-Kouz W, Mohd Nasir NA. Computational single phase comparative study of inclined MHD in a Powell–Eyring nanofluid. Heat Transf. 2021;50(4):3879–912.

[8] Avramenko AA, Kovetskaya MM, Shevchuk IV. Self-similar analysis of Eyring-Powell fluid in boundary layer without simplification. Chin J Phys. 2022;75:28–37.

[9] Chu YM, Nazir U, Sohail M, Selim MM, Lee JR. Enhancement in thermal energy and solute particles using hybrid nanoparticles by engaging activation energy and chemical reaction over a parabolic surface *via* finite element approach. Fractal Fract. 2021;5(3):119.
[10] Akram S, Athar M, Saeed K, Razia A, Muhammad T. Hybridized consequence of thermal and concentration convection on peristaltic transport of magneto Powell–Eyring nanofluids in inclined asymmetric channel. Math Methods Appl Sci. 2021.
[11] Aziz S, Ali N, Ahmad I, Alqsair UF, Khan SU. Contributions of nonlinear mixed convection for enhancing the thermal efficiency of Eyring-Powell nanoparticles for periodically accelerated bidirectional flow. Waves Random Complex Media. 2022;1–20.
[12] Patil VS, Patil AB, Ganesh S, Humane PP, Patil NS. Unsteady MHD flow of a nano powell-eyring fluid near stagnation point past a convectively heated stretching sheet in the existence of chemical reaction with thermal radiation. Mater Today: Proc. 2021;44:3767–76.
[13] Sohail M, Chu YM, El-Zahar ER, Nazir U, Naseem T. Contribution of joule heating and viscous dissipation on three dimensional flow of Casson model comprising temperature dependent conductance utilizing shooting method. Phys Scr. 2021;96(8):085208.
[14] Sohail M, Alrabaiah H, Nazir U. Radiative flow of MHD non-Newtonian fluid by utilizing the updated version of heat flux model under Joule heating. Heat Transf. 2021;50(4):3407–25.
[15] Waqas H, Imran M, Muhammad T, Sait SM, Ellahi R. Numerical investigation on bioconvection flow of Oldroyd-B nanofluid with nonlinear thermal radiation and motile microorganisms over rotating disk. J Therm Anal Calorim. 2021;145(2):523–39.
[16] Song YQ, Khan SA, Imran M, Waqas H, Khan SU, Khan MI, et al. Applications of modified Darcy law and nonlinear thermal radiation in bioconvection flow of micropolar nanofluid over an off centered rotating disk. Alex Eng J. 2021;60(5):4607–18.
[17] Imran M, Farooq U, Waqas H, Anqi AE, Safaei MR. Numerical performance of thermal conductivity in Bioconvection flow of cross nanofluid containing swimming microorganisms over a cylinder with melting phenomenon. Case Stud Therm Eng. 2021;26:101181.
[18] Wu J, Wu F, Zhao T, Antezza M, Wu X. Dual-band nonreciprocal thermal radiation by coupling optical Tamm states in magneto-photonic multilayers. Int J Therm Sci. 2022;175:107457.
[19] Zhou CL, Wu XH, Zhang Y, Yi HL. Super-planckian thermal radiation in borophene sheets. Int J Heat Mass Transf. 2022;183:122140.
[20] Khan U, Zaib A, Ishak A, Bakar SA, Animasaun IL, Yook SJ. Insights into the dynamics of blood conveying gold nanoparticles on a curved surface when suction, thermal radiation, and Lorentz force are significant: The case of Non-Newtonian Williamson fluid. Math Comput Simul. 2022;193:250–68.
[21] Imran M, Yasmin S, Waqas H, Khan SA, Muhammad T, Alshammari N, et al. Computational analysis of nanoparticle shapes on hybrid nanofluid flow due to flat horizontal plate *via* solar collector. Nanomaterials. 2022;12(4):663.
[22] Imran M, Kamran T, Khan SA, Muhammad T, Waqas H. Physical attributes of bio-convection in nanofluid flow through a paraboloid of revolution on horizontal surface with motile microorganisms. Int Commun Heat Mass Transf. 2022;133:105947.
[23] Farooq U, Waqas H, Muhammad T, Imran M, Alshomrani AS. Computation of nonlinear thermal radiation in magnetized nanofluid flow with entropy generation. Appl Math Comput. 2022;423:126900.
[24] Pushpa BV, Sankar M, Mebarek-Oudina F. Buoyant convective flow and heat dissipation of cu–h2o nanoliquids in an annulus through a thin baffle. J Nanofluids. 2021;10(2):292–304.
[25] Marzougui S, Mebarek-Oudina F, Magherbi M, Mchirgui A. Entropy generation and heat transport of Cu–water nanoliquid in porous lid-driven cavity through magnetic field. Int J Numer Methods Heat Fluid Flow. 2021;32(6):2047–69.
[26] Shafiq A, Mebarek-Oudina F, Sindhu TN, Abidi A. A study of dual stratification on stagnation point Walters' B nanofluid flow *via* radiative Riga plate: a statistical approach. Eur Phys J Plus. 2021;136(4):1–24.
[27] Mushtaq A, Mustafa M, Hayat T, Rahi M, Alsaedi A. Exponentially stretching sheet in a Powell–Eyring fluid: numerical and series solutions. Z Naturforschung A. 2013;68(12):791–8.
[28] Abrar MN, Uddin S, Akhtar K. Rheology of suspended hybrid nanoparticles in micro-rotating tangent hyperbolic fluid over a stretching surface. J Cent South Univ. 2023;30(4):1231–45.
[29] Samad Khan A, Abrar MN, Uddin S, Awais M, Usman I. Entropy generation due to micro-rotating Casson's nanofluid flow over a nonlinear stretching plate: Numerical treatment. Waves Random Complex Media. 2022;1–16.
[30] Abrar MN, Awais M. Rheology of alumina and silver nanoparticles over an exponentially stretching convective wall. J Comput Theor Nanosci. 2018;15(4):1373–8.
[31] Abrar MN, Sagheer M, Hussain S. Entropy formation analysis for the peristaltic motion of ferrofluids in the presence of Joule heating and fluid friction phenomena in a plumb duct. J Nanofluids. 2019;8(6):1305–13.
[32] Akhtar R, Awais M, Raja MAZ, Abrar MN, Shah SA, Yuan A, et al. Analytical treatment for the dynamics of second law analysis of Jeffery nanofluid with convective heat and mass conditions. J Nanoelectron Optoelectron. 2021;16(1):89–96.
[33] Abrar MN, Uddin S, Shah S, Razzaq R. Peristaltic heat transport analysis of carbon nanotubes in a flexible duct due to metachronal waves of cilia. Z Angew Math Mech. 2023;103(2):e202200066.
[34] Li S, Shaheen N, Ramzan M, Kadry S, Saleel CA. Thermophoretic particle deposition on double-diffusive Ree-Eyring fluid flow across two deformable rotating disks with Hall current and Ion slip. J Magn Magn Mater. 2024;589:171547.
[35] Das S, Tarafdar B, Jana RN. Modeling convective transport in a reactive fluid near a vertical pervious plate influenced by intense magnetic forces, induced magnetic field, Hall current and thermo-diffusion. Int J Mod Phys B. 2024;2550029.
[36] Ali A, Das S, Jana RN. Oblique rotational dynamics of chemically reacting tri-hybridized nanofluids over a suddenly moved plate subject to Hall and ion slip currents, Newtonian heating and mass fluxes. J Indian Chem Soc. 2023;100(4):100983.
[37] Nazir U, Mukdasai K, Sohail M, Singh A, Alosaimi MT, Alanazi M, et al. Investigation of composed charged particles with suspension of ternary hybrid nanoparticles in 3D-power law model computed by Galerkin algorithm. Sci Rep. 2023;13(1):15040.
[38] Bilal S, Asjad MI, Haq SU, Almusawa MY, Tag-ElDin EM, Ali F. Significance of Dufour and Soret aspects on dynamics of water based ternary hybrid nanofluid flow in a 3D computational domain. Sci Rep. 2023;13(1):4190.
[39] Kazmi SN, Hussain A, Rehman KU, Shatanawi W. Thermal analysis of hybrid nanoliquid contains iron-oxide (Fe_3O_4) and copper (Cu) nanoparticles in an enclosure. Alex Eng J. 2024;101:176–85.
[40] Fatima, N, Kousar, N, Rehman, KU and Shatanawi, W. Magneto-thermal convection in partially heated novel cavity with multiple heaters at bottom wall: A Numerical solution. Case Stud Therm Eng. 2023;43:102781.